Polyurethane-Encapsulated Mesoporous Carbon-Based Perovskite Solar Cells Resilient to Extreme Humidity and Mitigation of the Related Reversible J–V Bump

Published version:

DOI:10.1021/acsaem.4c02572

Polyurethane encapsulated mesoporous carbon-based perovskite solar cells resilient to extreme humidity and mitigation of the related reversible J-V bump

Salvatore Valastro[1], Gaetano Calogero[1], Emanuele Smecca[1], Valentina Arena[1], Giovanni Mannino[1], Corrado Bongiorno[1], Ioannis Deretzis[1], Giuseppe Fisicaro[1], Antonino La Magna[1], Simone Galliano[2], Gabriele Viada[2], Matteo Bonomo[2], Claudia Barolo[2] and Alessandra Alberti[1]**

[1]CNR-IMM zona industriale strada VIII n°5, 95121, Catania, Italy
[2]Department of Chemistry and NIS Interdepartmental Centre, University of Turin, 10125 Turin, Italy

**simone.galliano@unito.it*
**alessandra.alberti@imm.cnr.it*

Abstract

Mesoporous carbon-based (mC) hole-transporting-layer-free architectures offer a cost-effective solution for the commercialization of perovskite solar cells (PSCs). Adding 5-aminovaleric acid (AVA) to $MAPbI_3$ reduces defect concentration and enhances pore filling, while Eu enrichment in $CsPbI_3$ reduces cation migration and enables device reusability.

In this study, AVA-$MAPbI_3$ mC-PSCs were encapsulated at room temperature (RT) with a solvent- and water-free polyurethane (PU) resin. Under continuous ambient light, RT, and 40% relative humidity (RH), PU encapsulant acts as a barrier to extend device durability and enable reusability. The formation of a bump in the J-V curve after ~250 h, already reported at low scan-rate but here observed at 50 mV/s, strongly reduces the photovoltaic performances. We demonstrate that the bump is not linked to the formation of PbI_2 but is explained by a water-vacancy interaction that increases cation mobility and enhances screening effects near the electron-transport layer. The photovoltaic performances are fully restored by drying the devices under N_2 flow for ~48 hours.

A further addition of a hydrophobic Kapton tape interlayer between the PU and the device mitigates bump formation, boosts t_{90} to ~6000 h and projects t_{80} to ~10,800 h. Differently from the Kapton tape used alone, PU provides an effective sealing all around the devices, ensuring stability in 100% RH at 90 °C and even underwater.

For indoor applications, Eu:$CsPbI_3$ mC-PSCs typically degrade from γ- to δ-phase within ~1 h in air, whereas PU-encapsulated devices achieve t_{80} ~250 h, extendable to 1250 h with an additional closure glass slide.

Keywords: HTL-free PSC, durability, polyurethane, encapsulation, low-cost, J-V bump, water-resistant coverage

1. Introduction

Mesoporous carbon (mC) hole-transporting-layer-free (HTL-free) architectures represent a promising solution for the future commercialization of low-cost Perovskite Solar Cells (PSCs)[1,2] due to their printability, cost-effectiveness, and stability[3]. In addition, mC-PSCs offer versatility in integrating different perovskite formulations, with perovskite infiltration being the final processing step to complete the architecture. Besides outdoor use, mC-PSCs are also candidates for powering indoor photovoltaic Internet of Things (IoT) devices. [4]

Accounting for specific issues, the hybrid formulations like $MAPbI_3$ must face the undesired formation of volatile species during operation in air, while inorganic $CsPbI_3$ perovskite is unstable for the $\gamma-$ to $\delta-$ phase competition[5,6]. To extend the durability of $MAPbI_3$, additives such as aminovaleric acid (AVA) have been used[7]. Notably, mC-AVA-$MAPbI_3$ devices have demonstrated stability for up to 1000 h under continuous 1 Sun illumination, even without UV filters or external heating[8]. For $CsPbI_3$ perovskite, we have shown[9,10] that the addition of Eu inhibits the formation of defect states which populate the band-gap region, resulting in improved device performances. As a result, mC-PSC with integrated $CsPbI_3$:$EuCl_3$ shows good performance stability under continuous illumination at 55 °C in the N_2 environment[11].

However, despite being infiltrated into mC-PSCs, which offer humidity protection due to the hydrophobic character of the carbon electrode, all the perovskite compositions remain highly sensitive to ambient humidity. Therefore, for practical use, they require more effective protection with compatible encapsulating materials.

PSCs can be encapsulated using various methods, including the application of thin films (e.g. SiO_2[12], Al_2O_3[13]) or polymers (e.g. ethylene-vinyl acetate (EVA), polyolefin[14]) as protective coatings, with or without a cover glass[15,16,17,18]. In addition, edge sealants like polyisobutylene (PIB) can further slowdown moisture access from the edges[19]. An ideal encapsulation material should possess low oxygen (OTR) and H_2O vapour transmission rate (WVTR), ensuring minimal permeability to gases and moisture. It should maintain optical clarity without affecting light transmission (e.g. for building integrated photovoltaics[20,21], Agrivoltaics[22], Si/perovskite tandem solar cells[23]), although this may not be essential for applications where semi-transparency[24] is not required. Additionally, it should exhibit suitable mechanical properties to absorb strain[25], resist UV[26] and thermal oxidation[27], adhere strongly to the perovskite device/module, and not react with or degrade the perovskite. Moreover, its thermal expansion coefficient should be similar to that of the perovskite layer[28] to minimize the risk of delamination or mechanical stress-induced damage.

Various encapsulation strategies have been reported to encapsulate mC-PSCs, including glass covers with Surlyn edge sealing[29], thermoplastic resin films composed of ionomer-based materials with a glass cover[30,31], and the use of hot-melt polyurethane (PU) film with a glass cover[32]. Among these options, PU emerges as a promising encapsulation material[33] due to its cost-effectiveness, lightweight nature, and thermal and light stability. However, any encapsulation methods with glass covers increase the overall weight and costs of the device. Additionally, the sealing process with PU film requires a vacuum laminator with temperatures exceeding 80 °C and/or the application of pressure, which may damage the devices.

In this study, mC-PSCs infiltrated with AVA-$MAPbI_3$ have been encapsulated using a thermosetting PU resin coating, which has been previously used to successfully encapsulate traditional p-i-n PSC by some of us[34]. Liquid PU is prepared by mixing two precursor monomers (polyol and isocyanate) and deposited on mC-PSCs by the drop-casting method also compatible with industrial production. As a huge mainstay of the material, this liquid PU formulation without solvents or water content polymerize and adhere to mC-PSCs at room temperature in a nitrogen environment. Moreover, the process is easily up-scalable for large-scale production. The encapsulated devices were then stored in ambient conditions at relative humidity (RH) of 30-50%, continuously exposed to ambient light at room temperature. The photovoltaic performances of encapsulated devices were monitored over time, revealing a complex interplay between PU and ambient humidity, which results in the appearance of a reversible bump in the mC-PSC J-V curves. Typically, this bump is observed in unencapsulated mC-PSCs when the scan speed during J-V measurements is low (4-6 mV/s)[11,35]. We investigated through focused experiments and simulations the origin of this bump which arises in PU-encapsulated mC-PSCs at a higher scan speed (50 mV/s). In addition, focused encapsulation strategies (e.g. specific interlayer between PU and mC-PSC) were proposed to boost the durability of AVA-$MAPbI_3$ mC-PSCs along a timescale of 9 months, highlighting the pivotal role played by PU for protection and reuse in extreme humidity conditions and in H_2O soaking. Finally, the PU was applied to a full-inorganic Eu:$CsPbI_3$ perovskite. The performances of the encapsulated Eu:$CsPbI_3$ mC-PSCs were monitored, highlighting the positive effect of PU on improving solar cell durability.

2. Material and methods

Perovskite precursor solution fabrication: A mix solution of 1 M PbI_2 (Tokyo Chemical Industry) and 1 M CsI (Tokyo Chemical Industry) was prepared by mixing them in a mixed solvent of DMF and DMSO (3:1 v/v). $EuCl_3$ (Sigma-Aldrich) solutions of 0.1 M concentration were made in a mixed solvent of DMF and DMSO (3:1 v/v). The solutions were stirred at RT for 1 h. Then, 1 ml of the PbI_2/CsI solution was mixed with 0.5 ml of the $EuCl_3$ solution to obtain Eu:$CsPbI_3$ and then stirred for 1 h. The entire procedure is conducted in air (RH~35%). The AVA-$MAPbI_3$ precursor solution is commercially available (Solaronix).

mC-PSCs Fabrication: The layers of monolithic architecture are screen-printed on a fluorinedoped tin oxide (FTO) glass substrate and consist of a compact TiO_2(c-TiO_2) as hole blocking layer (~50 nm), a mesoporous TiO_2 (mp-TiO_2) as electron transporting layer (~500 nm), a mesoporous ZrO_2 (ZrO_2) as insulating layer (~1 mm) and a high temperature annealed carbon electrode (~10 mm). The entire stack is commercially available (Solaronix). Before the use, the sample was annealed at 400 °C for 30 min to remove contaminants trapped in the porous structure. The procedure of perovskite infiltration in mesoscopic stack was entirely conducted in a N_2- filled glovebox. For the fabrication of Eu:$CsPbI_3$ and AVA-$MAPbI_3$ mC-PSCs, we drop-casted 10.4 µl of Eu:$CsPbI_3$ solution and 5.76 µl of AVA-$MAPbI_3$ solution on the mesoporous stack by using a micropipette, respectively. We waited 30 min to allow the full infiltration of the solution. Then, for Eu:$CsPbI_3$ we perform two-step annealing 1) 90 °C for 10 min and 2) 350 °C for 2 min, followed by a rapid cooling at RT to form the γ-black photoactive phase. The addition of Eu in the form of $EuCl_3$ enhances the material's quality by reducing the formation of intra-gap defects[9]. For AVA-$MAPbI_3$ mC-PSC, we anneal the samples at 50 °C for 15 min to form the tetragonal photoactive phase.

Polyurethane Encapsulant Fabrication: Polyol and diisocyanate precursors were provided by Demak Polymers. Polyol resin with viscosity ~1300 Cp is composed by 80% Sovermol 780, 20% Polyol 3610, and 0.05% Tin-based catalyst, in weight. Diisocyanate resin with viscosity ~1100 Cp is composed by 40% Tolonate X Flo 100 and 60% Desmodur Eco N7300, in weight.

Aliphatic ether-ester based polyurethane is obtained by mixing polyol and diisocyanate (1:2.5 weight ratio) for 5 min at RT. Prior to deposition, the mixture is subjected to a vacuum treatment to eliminate the air bubble and the humidity trapped during mixing process. The PU mixture has a gel time of 45 min. PU is thus deposited by drop-casting 600 μL within a square frame delimiting the deposition area onto the mC-PSC to constrain the PU to the designated cell area, ensuring reproducible thickness in different samples (1.5±0.2 mm). The PU thickness measurements show a variation of +2% from center to borders in a sample. Photovoltaic performance over time on samples with different PU thickness (1.3 ÷1.7 mm), are similar, suggesting that such differences in PU thickness do not have effect. The PU/mC-PSC is stored at RT and in N_2 environment for 3 days to allow the complete polymerization of the encapsulant layer avoiding intrusion of air humidity. The resulting PU film has hardness of 63 ShD, and glass transition temperature of 33 °C.

X-Ray Diffraction: XRD patterns were collected using a SmartLab (Rigaku) diffractometer equipped with a 9kW rotating anode Cu x-ray source (operating at 45 kV and 200 mA) and HyPix3000 detector. An Anton Paar heating stage, equipped with a polyether ether ketone dome filled with dry N_2 at a pressure slightly above the atmospheric one (+0.3 bar), was used to keep the samples at controlled temperatures (24 °C) in controlled atmospheres. The step size for pattern recording was 0.02° with acquisition speed equal to 1°/min.

Device characterization: J-V characteristics were measured in air by a digital source meter (Keithley model 2401) under AM 1.5-simulated sunlight (100 mW/cm^2) from Peccell PEC-L01. The solar cells devices were masked (shadow mask) to define the active area of 144 mm^2. The scan range was from −0.1 to 1.2 V for forward scan and from 1.2 to −0.1 V for reverse scan with a step of 0.01 V with a scan rate of 50 mV/s.

SEM images: SEM-FIB analyses were performed by dual beam focused ion beam (FIB) using a Thermofisher Helios 5 UC+ system. Before the SEM-FIB analysis most part the carbon layer was mechanically removed. FIB cross section was performed with the Ga+ ion beam at 30 keV, down to the glass substrate, in regions where the residual carbon layer was more than 4 μm. Tungsten protective layer was deposited in situ to avoid excessive damage from the ion beam. Several cross sections were done in every sample in order to confirm the local results. In the sample exposed to water every FIB cross section has met a dissolved region until the oxides layer. No one dissolved area was found in the PU encapsulated sample. SEM images were acquired with a back-scattered electrons configuration, using 5 keV electron beam.

Density functional theory calculations: We used the density functional theory to calculate the total energy of H_2O molecules within $MAPbI_3$ crystals with positively charged iodine vacancies (V_I^+). We considered (2×2×2) pseudocubic $MAPbI_3$ supercells containing a single H_2O molecule and one V_I^+ defect and various positions within the supercell. The ground state energy of this system was calculated with the aid of the Quantum Espresso software suite[36], using the vdw-DF3-opt1 van der Waals exchange-correlation functional[37] along with Perdew-Burke-Ernzerhof ultrasoft pseudopotentials[38,39] for the description of core electrons. The cutoff for the kinetic energy for wavefunctions and the augmented charge density were set to 50 Ry and 400 Ry, respectively. We used a (4×4×4) Monkhorst-Pack grid for the sampling of the Brillouin zone[40], whereas both atoms and lattice parameters were allowed to fully relax.

3. Results and discussion

3.1 Polyurethane on mC-PSCs with AVA-MAPbI$_3$

3.1.1 Understanding the role of PU at the interface with the device

We investigated the PU barrier capability when it is deposited on mC-PSCs infiltrated with standard AVA-$MAPbI_3$ which was optimised for this architecture to be stable for >1000 h in air under full sunlight.[7] Specifically, as the final step after perovskite infiltration, a 1.5±0.2 mm-thick layer of PU is deposited by drop-casting a mixture of polyol and diisocyanate (1:2.5 ratio) onto the mC-PSC surface (see Fig. 1 a-b) in ambient conditions. Then, the PU is left to polymerize for 3 days under dry N_2 flux at RT. The detailed synthesis of PU and fabrication steps of PSCs are provided in the Experimental Section. We compare the evolution of photovoltaic parameters over time of the reference unencapsulated device (Fig. 1a), the encapsulated device with PU (Fig 1b) and the device encapsulated with PU but with an additional C tape layer placed between PU and the device surface (C tape+PU) (Fig.1c), all of them continuously exposed to air (RH 30-50%) and ambient light (300-1500 lux) at RT. The latter encapsulation strategy is used to decouple the presence of PU from that of mC-PSC, to evaluate eventual PU-Perovskite interaction effects. Figures 1d–f show the evolution of J-V curves over 1500 hours for the representative devices from batches of four samples per type. Figures 1g–j illustrate the corresponding changes in photovoltaic parameters over time. Statistical data, represented as box plots of photovoltaic parameters, are shown in Figure S1. The unencapsulated device shows an initial efficiency value of 5.6% in agreement with values reported in the literature[11,41] for the same large-area (1.5 cm^2) device architecture without additional humidity thermal treatments[41]. Higher efficiency values (in the range 11-14%) are reached on small-area devices (0.04 to 0.1 cm^2)[11,42]. The unencapsulated device shows an initial improvement of efficiency ascribable to an open-circuit voltage (V_{OC}) increase from 0.85 to 0.91 V in the initial days, as shown in Fig. 1d, and to a small increase of the short-circuit current (J_{SC}), which stabilizes to an average value of 12.5 mA/cm^2.

On the contrary, the fill factor (FF) value remains stable over time at ~50%. Then, the power conversion efficiency (PCE) remains almost unchanged, at a value of ~6% up to 1500 h, as well as the other photovoltaic parameters. The performances of PU and C tape+PU devices show similarities but diverge in evolution over time if compared to unencapsulated PSCs. Initially, the J_{SC} values align with those of the unencapsulated device (12.5 mA/cm^2), while V_{OC} and FF values are lower compared to unencapsulated PSCs (Fig. 1g-h), similar to what is reported in the literature for different encapsulation strategies in the same mC-PSCs architecture[31]. However, both V_{oc} and FF rise throughout ~200 h, eventually almost matching those of the unencapsulated device, as observed in J-V curves at day 9 in Fig. 1 d-e-f and in Fig.1g-h-i-j. The PU and C tape+PU covered devices reach the maximum value of efficiency of ~5% after ~250 h.

After 250 h of storage, a distinctive bump appears in the J-V curves of both PU and C tape+PU PSCs causing a decrease in J_{sc} and an increase in FF (see Fig. 1e-f). Specifically, the PU device exhibits a high FF of ~70% and J_{SC} of 5 mA/cm^2 from 250 h until 1500 h, whereas the C tape+PU device shows an increasing FF value from 45% to ~60% and J_{sc} of 7.5 mA/cm^2. During this period, the V_{OC} values remained stable, except for a noticeable increase in V_{OC} observed in the PU PSC ~1000 h (Fig 1g). This trend of photovoltaic parameters badly impacts the device efficiency values after 1500 h of the C tape+PU mC-PSC (3.9%) and the PU mC-PSC (3%). Bumps were observed in identical unencapsulated device architectures (see Fig, S2)[11] but only at a low scan rate (6 mV/s instead of 50 mV/s), and therein related to cation migration. The comparison of the J-V curves in which the bump appears, is reported in Fig. S2, also showing that in the J-V curve of the C tape+PU encapsulated device at 6 mV/s, no bump emerged. This aspect will be further discussed in section 2.2.2.

Thus, we investigate the origin of this behaviour for PU-encapsulated devices. The hypothesis of a degrading interaction between the PU and the device surface or between the C tape adhesive and the device surface can be excluded, since we found that the mC-PSC with only C tape on the device (w/o PU) behaves over time as the unencapsulated device, i.e. with no bump formation as shown in Fig. S3.

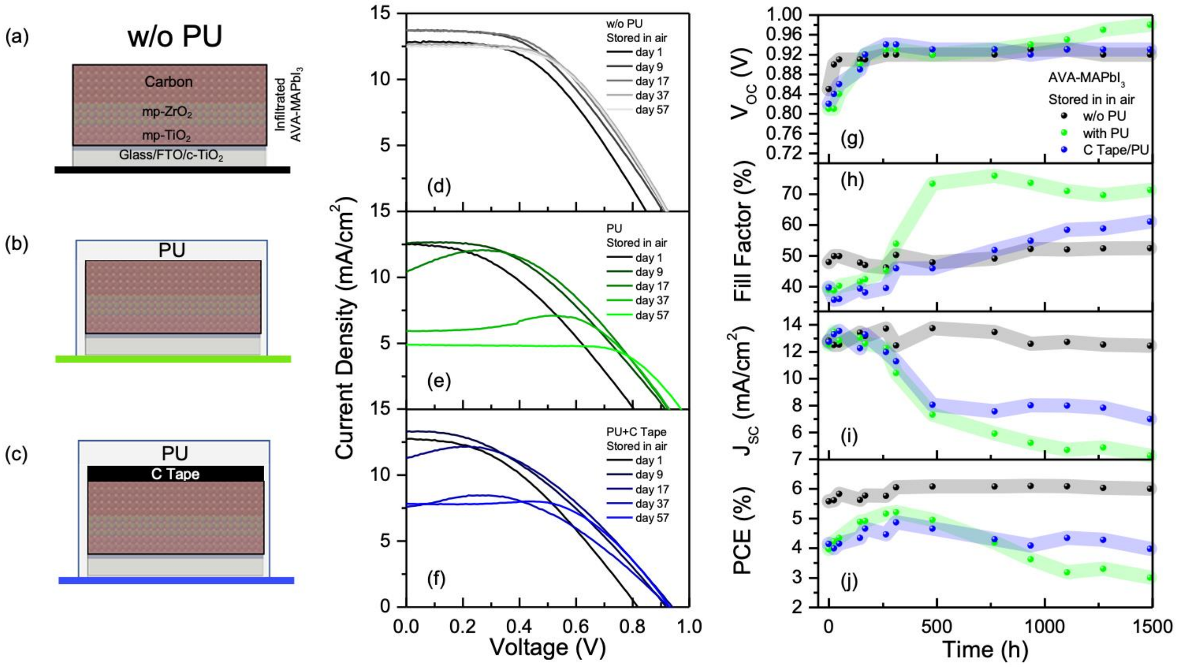

Fig.1 Schematic of the AVA-MAPbI$_3$ mC-PSC w/o PU (a), with PU (b), and with C tape+PU (c). J-V curves (reverse scan) over the time for AVA-MAPbI$_3$ mC-PSC w/o PU (d), with PU (e) and with C tape+PU (f). Evolution of V_{OC} (g), FF (h), J_{SC} (i) and PCE (j) over the time for AVA-MAPbI$_3$ mC-PSC w/o PU, with PU and with C tape+PU.

To investigate the structure of mC-PSC under the PU layer after 1500 h exposure to air, we peeled off the PU and the C tape + PU layer and performed X-ray diffraction (XRD) measurements on the mC-PSCs at the side of the carbon layer (Fig 2a). We performed XRD measurements on unencapsulated mC-PSC as a reference. In the case of the PU device, the peeling process removed almost all the mC-Perovskite (mC-PSK) layer from the substrate whilst in the case of C tape+PU device only a thin layer was removed. For this reason, we performed the analysis on both the mC-PSC remained on one side after peeling and the peeled PU from the other mC-perovskite side. Surprisingly, despite the good performances, the unencapsulated sample exhibited a dominant peak at 12.67° which indicates the presence of PbI$_2$, a by-product diagnostic of MAPbI$_3$ degradation, and a minor peak at 14.1° (MAPbI$_3$ β-tetragonal phase) (Fig. 2b). This finding contrasts with the PSC performance which does not show any decay being stable at a value of ~6% (see inset of Fig. 2b). We argue that the degradation is a progressive process that starts at the mC-side of the device, the one exposed to air, and proceeds downwards. This transformation does not initially impact the electrical performances that are instead linked to the inner perovskite infiltrated into the mesoporous oxides (i.e. ZrO$_2$ and TiO$_2$) where carrier photogeneration mostly happens (see simulated generation rate profile in Fig. S3). This is confirmed by XRD measurements at grazing incidence angle (0.4°) in Fig. S5, which shows how in the topmost 600 nm of the mC/perovskite blend only PbI$_2$ is present, with the MAPbI$_3$ peak appearing at a 1.2 μm depth. It is important to recall that PbI$_2$ is a hydrophobic material, and thus its presence as a capping layer can slow down further access of moisture thus delaying device degradation[43].

The C tape + PU mC-PSC displays a different pattern compared to the unencapsulated device, featuring a prominent MAPbI$_3$ peak alongside a minor presence of PbI$_2$. Similarly, the XRD analysis of the PU-encapsulated device reveals only the MAPbI$_3$ peak at 14.1°, with no detectable PbI$_2$ in either the mC-PSC post-peeling or the peeled PU (mC/perovskite side). In addition, no peaks of hydrated phases (monohydrated or dihydrated $MAPbI_3$) are detected[44] (Fig. S6). This underscores the protective role of PU in shielding $MAPbI_3$ from irreversible degradation into PbI_2. All those findings suggest that the decay of performances for PU samples is not related to an irreversible degradation of $MAPbI_3$ layer into PbI_2, but to a different phenomenon. Moreover, we found that after C tape+PU peeling, the bump vanished (Fig. S7) and the J_{SC} increased, reinforcing the hypothesis that the phenomenon of performance decay is reversible and that the bump is related to the presence of PU (since the devices with C-tape alone w/o PU have never shown a bump).

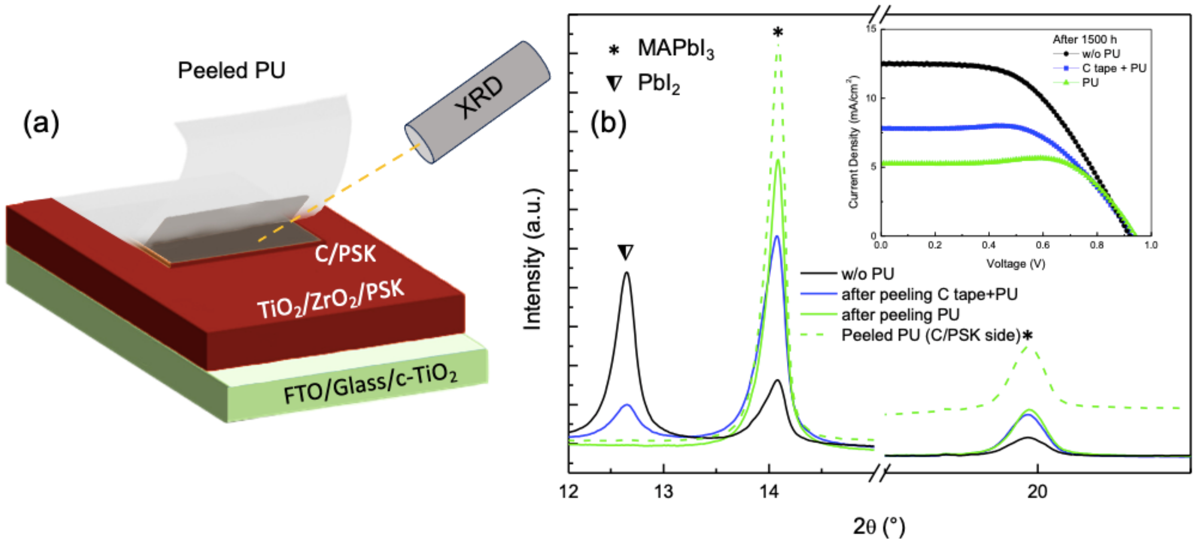

Fig.2 (a) Schematic of X-Ray diffraction measurements on AVA-$MAPbI_3$ mC-PSCs in which the PU layer is peeled off. (b) X-ray diffraction patterns of AVA-$MAPbI_3$ mC-PSCs w/o PU and after peeling of PU and C tape+PU. In the inset, the J-V curves after 1500 h of storage in air for the three kinds of devices are shown.

3.1.2 Understanding the role of PU with respect to air humidity

To disentangle the role of ambient humidity, we prepared two mC-PSCs encapsulated with PU and two encapsulated with C tape+PU. One pair of devices was initially stored in air, while the other was stored in a N_2 flow environment (see Fig. 3a). After one month, the samples stored in air were transferred to N_2, and vice versa (Fig. 3a), followed by another change of storage conditions after an additional month. Fig. 3b-c-d-e illustrates the evolution of photovoltaic parameters for PU devices, while Fig. 3f-g-h-i depicts those for C tape+PU mC-PSCs, with storage conditions alternating between air (circular markers) and N_2 (triangular markers).

Focusing on the first 700 h of the experiment, we observe that the V_{OC} values for both mC-PSCs encapsulated with PU and C tape+PU increase over time when stored in air (from 0.86 V to 0.91 V). Conversely, when the samples are stored in N_2, the V_{OC} decreases from 0.86 V to around ~0.78 V. The PU and C tape+PU devices stored in air exhibit the same behaviour as observed previously, with a bump emerging after several days, resulting in an inflated FF and a decrease in J_{SC}. In contrast, no bump is found in the J-V curve of devices stored in N_2, thus the values of FF and J_{SC} remain constant over time.

After the change of the storage conditions (700-1400 h), the devices previously stored in N_2, now in air, show an increase in V_{OC} from 0.78 V to 0.92 V, accompanied by the emergence of the bump after several days (increased FF and decreased J_{SC}). Conversely, the samples previously stored in air, now in N_2, demonstrate a complete recovery of the performances after 1-3 days in N_2, particularly with an increase in J_{sc} and a decrease in FF, reflecting the disappearance of the bump in J-V curves. It's noteworthy that the V_{OC} for the sample stored in N_2, after 800 h in air, slightly decreases but remains at a high value in the range ~0.86-0.88 V, indicating that the increase of V_{OC} is related to a maturation process occurring when the sample is stored in air for the first time, similarly to what was observed in the literature[59]. The last change of storage conditions (1400-2100 h) for both mC-PSCs confirms what was previously observed.

In summary, the appearance of bumps with the consequent inflation of FF and decrease in J_{SC} is a phenomenon occurring in the air, probably due to limited moisture access through the PU, to an extent small enough to allow a full reset through storage in N_2 for 1-3 days. A drying process thus enables H_2O molecules to leave the device in both cases, whether or not the PU is in direct contact with the mC-PSC.

The optimal approach would be to prevent or minimize bump formation through targeted strategies, such as incorporating interlayers into the device structure (as further discussed below) or, in certain applications like double-glazed windows, using an inert gas environment between glass layers to reduce exposure to moisture and oxygen.

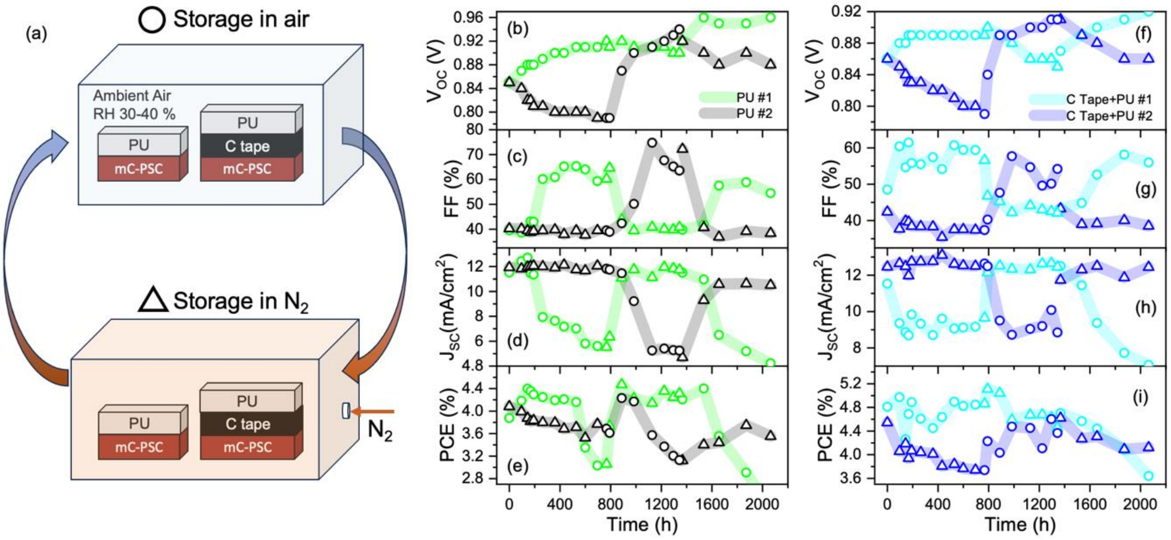

Fig. 3 Schematic of the experiment in which one couple of AVA-MAPbI$_3$ encapsulated devices with PU and with C tape+ PU was initially stored in air, while the other was stored in a nitrogen (N_2) environment After one month, the samples stored in air were transferred to N_2, and vice versa followed by another change of storage conditions after an additional month (a). Evolution of V_{OC} (b), FF (c), J_{SC} (d) and PCE (e) over the time for PU encapsulated AVA-MAPbI$_3$ mC-PSCs with storage conditions alternating between air (indicated by circular marks) and N_2 (indicated by triangular marks). Evolution of V_{OC} (f), FF (g), J_{SC} (h) and PCE (i) over the time for C tape+PU encapsulated AVA-MAPbI$_3$ mC-PSCs with storage conditions alternating between air (indicated by circular marks) and N_2 (indicated by triangular marks).

3.1.3 Understanding the role of the PU under high humidity conditions

The influence of H_2O vapour on the formation of the bump in the J-V curve was investigated through a focused experiment in which the unencapsulated mC-PSC surface was intentionally exposed to H_2O vapour (see Fig. 4a). The sample was placed in a closed glass container filled with 60 mL of water at RT, serving as a source to generate a humidity-saturated environment (100% RH). The device surface was positioned 3 cm away from the water, and the glass side was masked to allow light illumination of the mC-PSC. The J-V curve before exposure to H_2O vapour is depicted in Fig. 4b. Following only 1 min of exposure to H_2O vapour at RT, a bump emerged with a significant decrease in J_{SC} and inflation in FF. The forward and reverse scans of this J-V curve closely resembled those of the mC-PSC encapsulated with PU after 37 days of storage in air, as illustrated in Fig. 4c. Subsequent exposures of 10, 20, and 30 min to H_2O vapour do not eliminate the bump, instead, it slightly shifts towards lower voltage values. Upon removal of the H_2O vapour source, the bump promptly vanishes, with a slight increase in J_{SC}, although it does not return to its initial value.. Attempts to recover performance by storing the sample in N_2 environment have resulted in an initial but partial increase in J_{SC} after 3 h, but further recovery was not achieved after an additional day in N_2. Exposing the same device to a further 1.5 h of H_2O vapour results in the bump reforming. Once again, after 3 days of N_2 storage, only a partial recover of performance is observed (Fig S8), and the mC-PSC performance is permanently compromised. In this case, no PbI_2 or hydrated phase were detected by XRD measurements after the stress test, as shown in Fig. S9.

The same experiment was conducted using the mC-PSC encapsulated with C tape+PU (Fig. 4d). Differently from the previous case (w/o PU), exposure to H_2O vapour for 19 h at RT does not induce any efficiency changes in the mC-PSC, and bumps are not formed. Only a slight increase in V_{OC} was detected. To enhance the water action, the temperature was raised to 50 °C, thus elevating the H_2O vapour pressure inside the glass to 92.5 torr from 22.4 torr at 24 °C [45]. After 80 min, the bump starts to appear. Further increasing the temperature to 90 °C (vapour pressure raised to 525.8 torr) results in the full formation of a bump after 25 min. As a note of merit, after 1 day of N_2 storage, the electrical performance was fully recovered. A similar experiment was conducted with the water temperature fixed at 90 °C. As shown in Fig. 4f, 3 h were required for the complete appearance of the bump. However, full performance recovery was achieved, even in this case, after 1 day of N_2 storage. The experiment demonstrates that the bump phenomenon is induced by exposing the unencapsulated device to medium-pressure H_2O vapours or, in the case of encapsulated devices, its appearance is promoted through prolonged exposure and increased vapour pressure at elevated water temperature. To further investigate the interaction between PU film and water, the water absorption has been evaluated by dipping the PU film in deionized water at room temperature for prolonged time. The results showed that PU film absorbs around 0.8% by weight of water after 7 hours (Fig. S10), indicating a certain amount of water can permeate and be retained into the polymer matrix. Those outcomes validate the hypothesis that water diffuses through the PU resin and mediates a moderate access of single water molecules at the interface with the device, lastly causing the J-V bump. Limited access of water molecules also explains the reversibility of the electrical performances that occurs after drying the device under N_2 flow.

Since no degradation by-products were found in XRD analyses in encapsulated PSCs, we can further support our argumentation by citing the following literature findings. Schlipf et al.[46] showed that under ≤58% RH, water molecules progressively adsorb onto the surface of $MAPbI_3$ crystals until the film contains ~10 vol % of water; for this humidity level the H_2O vapour pressure is not sufficient to enter the crystals and to form monohydrate phase and indeed no hydrated phases or PbI_2 were detected. Fransishyn et al. [47] demonstrated that cell failure in humid environments is not caused by the decomposition of the perovskite layer, but rather by an increased ionic mobility[48] within $MAPbI_3$. This elevated mobility results in the loss of photocurrent due to the screening of the built-in potential in device architecture with gold as the top electrode. Interestingly, they also observe the emergence of bumps in J-V curves under this condition. Leguy et al.[44] observed a similar behaviour in $MAPbI_3$-PSC devices after 3 h at 77% RH at 21 °C, consisting of a J_{sc} decrease and a progressive bump appearance followed by a recovery of performance by N_2 flowing for 5 h; consistently PbI_2, hydriodic acid (HI) and CH_3NH_2 were not detected as instead typically observed in the presence of water. However, that paper and the related results refer to layered device architectures that are probed at high scan rates (e.g. 500 mV/s [44]). In our case, $MAPbI_3$ is used in a mesoporous architecture that is, in principle, more accessible to water. A recent paper[49] reported a bump in experiments under water-rich environment conditions but under low scan rates (4.2 mV/s), although an interpretation of the origin of the bump and its relationship with water is not provided.

Based on all those findings and our experiments we argue that limited access of water molecules mediated by PU that, intercalating in the $MAPbI_3$ grains, can thus increase the ionic mobility with fingerprint in the bump formation. Consistently, when the PU is peeled off, the bump disappears (Fig S7). Similarly, storing the device in a flowing N_2 environment enables water molecules release from the perovskite and the PU layer, with the performances consequently recovered (Fig 4e-f).

In unencapsulated devices, we show that J_{SC} is not fully recovered after storage in N_2. It was reported in Ref. 50 that the hydration/dehydration process without any encapsulation could induce morphological alterations in the recrystallized $MAPbI_3$ grains, with irreversible effect on the J_{SC}. Conversely, in Ref. 46, it is reported that $MAPbI_3$ morphology changes from faceted to more round-shaped crystals after exposing it to 1.5 h of H_2O (RH ~80-100%). In our case, scanning electron microscopy analyses performed on the cross-sections of unencapsulated mC-PSC after water exposure (Fig. 5a) reveal large areas extending from the carbon layer to the oxides (mp-TiO_2 and mp-ZrO_2), wherein the perovskite is missed as indicated by the change in mass contrast (in Fig. 5a bright regions identifies infiltrated perovskite material). The funnel shape of those altered regions denotes abundant access of water into the mC layer that further extends into the mp-ZrO_2 and mp-TiO_2 layers. This explains the irreversible loss in J_{SC}.

This effect is not found in PU-encapsulated mC-PSCs (Fig. 5d) and indeed, as a note of merit, this coverage works against abundant water access even at extreme conditions of water pressure and temperatures, for the benefit of a full recovery of performances. Extreme humidity conditions at high environmental temperatures (40-90 °C) were also applied in Ref. 49 onto the same mC-PSC devices by using super-repellent nanoparticles, that were instead not sufficient to preserve the device from degradation.

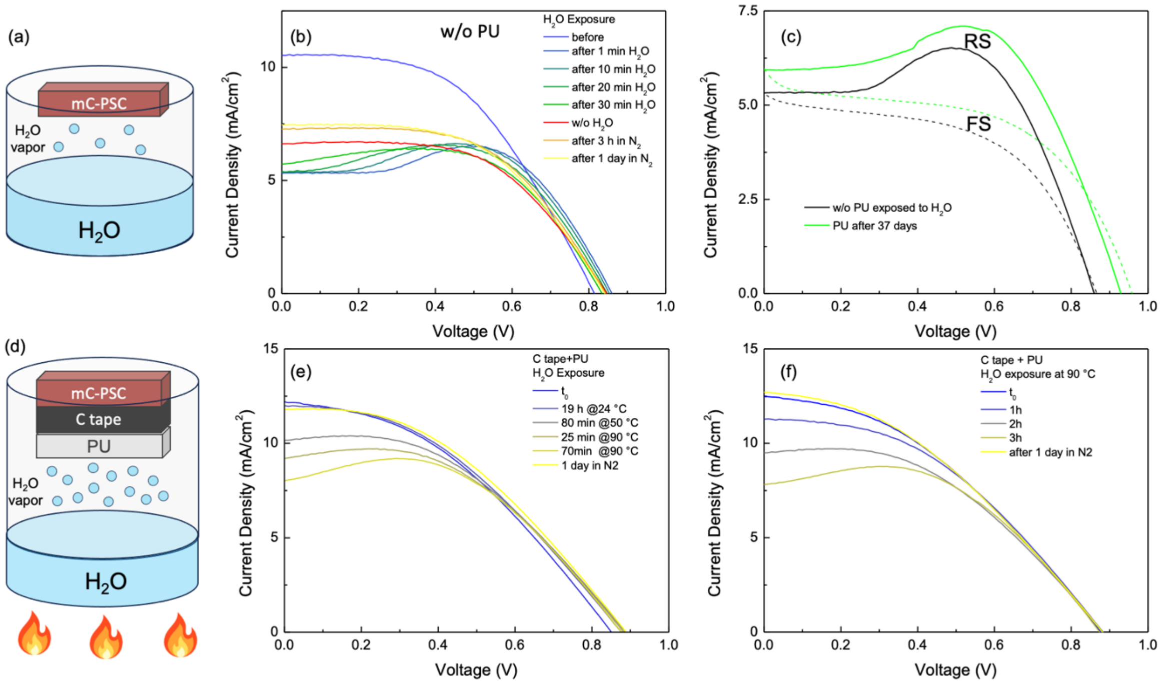

Fig. 4 Schematic of the experiment where the unencapsulated AVA-$MAPbI_3$ mC-PSC surface is exposed to extreme humidity conditions at RT (a). J-V curves of the unencapsulated AVA-$MAPbI_3$ mC-PSC before and after cycle of H_2O exposure or N_2 storage for several days (b). Comparison of J-V curve of unencapsulated AVA-$MAPbI_3$ mC-PSC exposed to H_2O and PU encapsulated AVA-$MAPbI_3$ mC-PSC after storage in air for 37 days (c). Schematic of the experiment where the C tape+PU encapsulated AVA-$MAPbI_3$ mC-PSC surface is exposed to H_2O vapour at RT and at higher temperatures (50 °C and 90 °C) (d). J-V curves of the C tape+PU encapsulated AVA-$MAPbI_3$ mC-PSC before and after cycle of H_2O exposure or N_2 storage for several days at RT and higher temperatures (e-f).

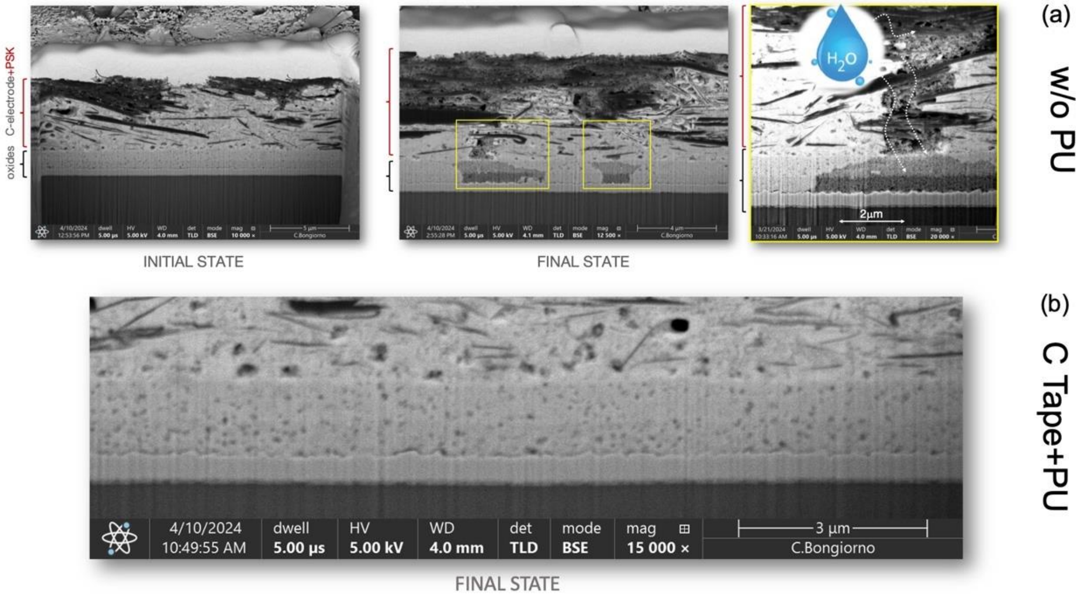

Fig.5 (a) Scanning electron microscopy analyses performed on unencapsulated mC-PSC before (initial state) and after (final state) water exposure. (b) Final state of encapsulated mC-PSC after exposure to extremes humidity conditions at high environmental temperatures.

3.2 Understanding the origin of the bump in the J-V curves

3.2.1 Influence of PSC-PU interface on the bump

To address the origin of the bump in J-V of PU-encapsulated devices over time, we fabricated new devices (4 of each kind) using different interlayers between mC-PSCs and PU. Specifically, we used standard adhesive-backed Kapton tape and a bilayer made of Al foil and C tape. Fig. 6a-b-c displays the J-V curves over time of the PU, C tape+PU, and solely C tape encapsulated devices, serving as references, consistent with those previously presented in the paper. Figures 6c–f illustrate the time evolution of the J-V curves for the representative mC-PSC from a batch of four devices per type, with the corresponding photovoltaic parameters shown in Figures 6g–j. Statistical data of photovoltaic parameters are provided in Figure S11. The mC-PSC covered with Kapton tape+PU exhibits a distinct behaviour over time: a small bump appears after ~250 h, but after ∼1000 h it begins to diminish until it disappears, as shown in Fig. 6d. Conversely, the behaviour of the C tape+Al foil+PU resembles that of the C tape+PU device, while the Al foil+C tape+PU mC-PSC behaves similarly to the Kapton tape+PU device. The photovoltaic parameters over time shown in Fig. 6g-h-i-j indicate that at the end of the monitoring period (1500 h), the parameters of the Al foil+C tape+PU and Kapton tape+PU mC-PSCs are similar to those of the C tape and unencapsulated devices (see Fig. 1). In particular, J_{SC} and FF values are ~12.5 mA/cm^2 and 50%, respectively, characteristic of a J-V curve without a bump. As a result, the PCE for these devices (C tape, Al foil+C tape+PU, Kapton tape+PU) is in the range of 5-6%, while for the other devices (PU, C tape+PU, C tape+Al foil+PU) is in the range of 3-4%. The fact that the C tape+Al foil+PU and Al foil+C tape+PU behave in different ways indicates that the interface with the mC-perovskite surface is a key factor. We argue that under the Kapton tape or the aluminum foil, a low H_2O permeability is achieved because of their higher hydrophobicity and water barrier properties compared to PU and C tape+PU. This would be in agreement with the different water contact angles on the three different surfaces, as shown in Fig. S12. In particular, the surfaces of PU, C-tape, and Kapton tape exhibit contact angles of 75.9°, 89.3°, and 92.5°, respectively (Table S1). The initial bump formation in the samples covered with Al foil+C tape+PU and Kapton tape+PU, which is suppressed over time, can thus be linked to limited water molecules trapped at the interface as the coverage is applied during the in-air procedure.

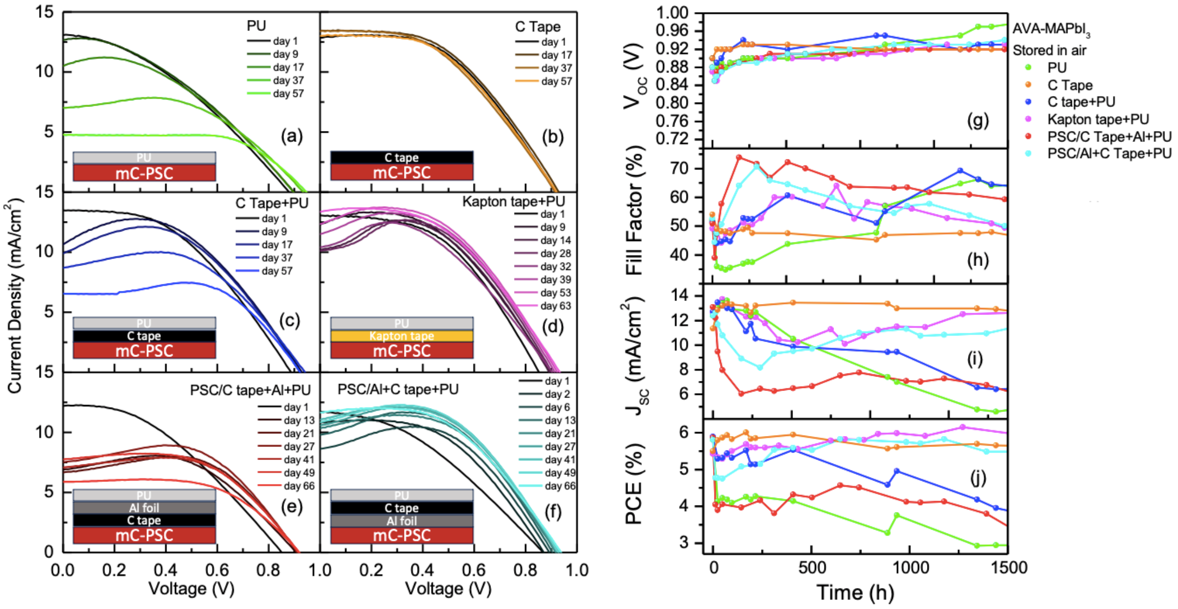

Fig. 6 Schematic and J-V curves (reverse scan) over the time for AVA-$MAPbI_3$ mC-PSC with PU (a), C tape (b), C tape+PU (c), Kapton tape+PU (d), C tape+Al+PU (e) and Al+C tape+PU (f). Evolution of V_{OC} (g), FF (h), J_{SC} (i) and PCE (j) over the time for AVA-$MAPbI_3$ mC-PSC with PU, C tape, C tape+PU, Kapton tape+PU, C tape+Al+PU and Al+C tape+PU.

The behaviour of the Kapton tape+PU mC-PSC was monitored over a longer time and compared to the unencapsulated device. As shown in Fig. 7a-b-c-d, the t_{90} of unencapsulated AVA-$MAPbI_3$ mC-PSC, calculated relative to the maximum value reached by the PSC (6.25%), is equal to 1965 h. The t_{90} of the Kapton tape+PU mC-PSC is equal to ~6000 h (maximum PCE value of 6.15%). Fig. 7e-f shows the mC-PSCs at t90 with Kapton+PU encapsulation and without encapsulation showing the effect of PU in avoiding the $MAPbI_3$ to PbI_2 transformation.

Once reached the t_{90}, the Kapton tape+PU mC-PSC was further stressed under 100% RH H_2O vapour at 90 °C for 3 h, as done for the C tape+PU case (Fig. 7g and Fig. 4d). Despite this harsh treatment, only a slight decrease in J_{sc} was observed, with no bump effect, differently to what was seen with C tape+PU coverage. This observation supports the hypothesis that the small bump detected in the initial days for the Kapton tape+PU-encapsulated mC-PSC, which later disappeared, is due to water molecules trapped during sample preparation under ambient conditions. This underlines that the Kapton tape+PU encapsulation minimizes the H_2O entrance and its interaction with the perovskite. Like the C tape-PU case, one day in N_2 results in the recovery of the initial J_{SC} value. Furthermore, the same Kapton tape+PU covered device, after H_2O vapour exposure, was subjected to a full soaking in liquid H_2O at RT. Remarkably, the Kapton tape+PU effectively protected the mC-PSC, preventing the transformation from $MAPbI_3$ to PbI_2 (Video S1), allowing the preservation of mC-PSC performance as shown in Fig. 7h (10 s and 30 s soaking). In contrast, the unencapsulated device transforms from $MAPbI_3$ into PbI_2 after 5 s of soaking in water (Video S1), resulting in complete performance loss, as shown in Fig. S13. The experiment demonstrates that the PU creates effective coverage and sealing all around the device that assures its stability even under extreme conditions.

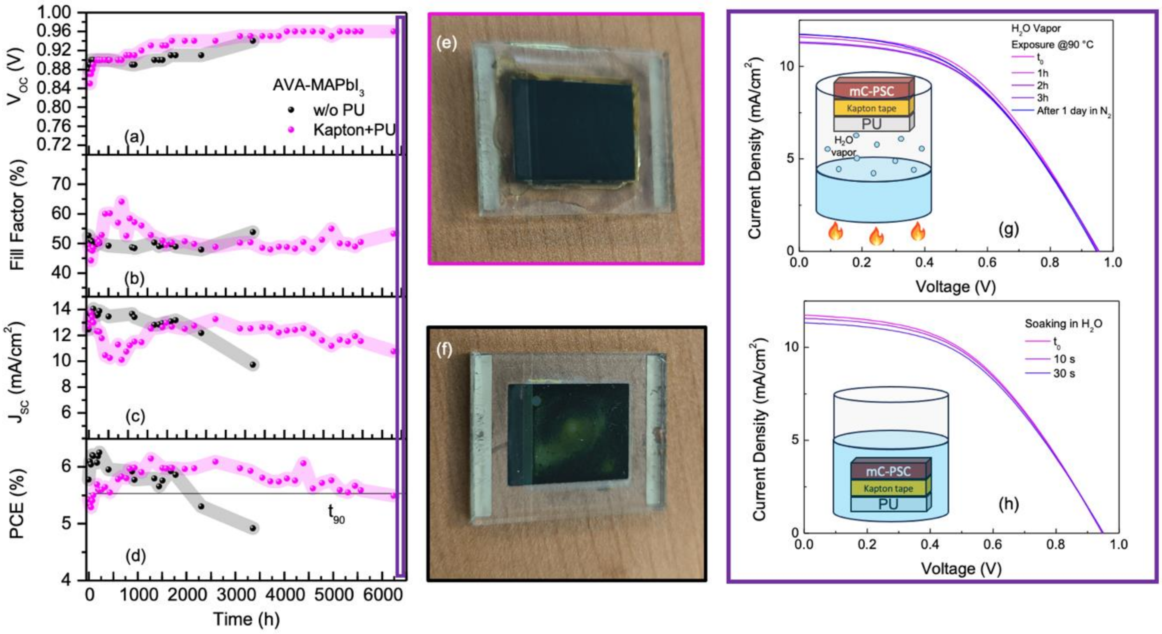

Fig 7 Evolution of V_{OC} (a), FF (b), J_{SC} (c) and PCE (d) over the time for AVA-MAPbI$_3$ mC-PSC encapsulated with Kapton tape+PU. Photo of the mC-PSC encapsulated with Kapton tape+PU and unencapsulated one at t_{90}. Photo of the mC-PSC encapsulated with Kapton tape+PU (e) and unencapsulated one (f) at t_{90} (g) J-V curves of AVA-MAPbI$_3$ mC-PSC encapsulated with Kapton tape+PU before and after cycles of H_2O exposure (100% RH) at 90 °C. (h) J-V curves of AVA-MAPbI$_3$ mC-PSC encapsulated with PU+Kapton tape before and after cycles of soaking in liquid H_2O at RT.

3.2.2 Influence of the ionic mobility on the bump

A bump in the reverse J-V curves of PSCs has often been observed or predicted[44,47,49,51] , however, its microscopic physical origin, especially its possible connection with water, is still not conclusively understood. A recent study[51] proposed that the bump appearing in mC-PSC with infiltrated MAPbI$_3$ and its dependence on voltage scan rate may be attributed to a relaxation mechanism from a metastable state at high scan rates to a stable one at lower scan rates, where charge transfer at the contacts is suppressed, although this could not be ascribed to ion migration, nor possible interactions with water. Theoretical studies on layered PSCs have predicted that water molecules intercalated in MAPbI$_3$ (embedded in the perovskite lattice without disrupting it) reduce the energy barrier for the migration of positively charged iodine vacancies (i.e., the most mobile defects in MAPbI$_3$ [52]), thus enhancing their mobility[53], with the specific value of the barrier strictly dependent on the particular ab-initio description[54]. With this in mind, we decided to simulate the reverse-scan J-V curve of mC-PSCs infiltrated with MAPbI$_3$ using the commercial tool Setfos (v5.4.13; by Fluxim AG)[55], accounting for light absorption and mixed electronic and ionic conduction in a transient drift-diffusion framework. Our goal was to demonstrate that the bump and the decrease in J_{SC} is triggered by the water-induced increase in cation mobility.

The device layout and simulation parameters are identical to those reported in Ref. 11, where the unencapsulated mC-PSC architecture with MAPbI$_3$ was modelled and optimized to reproduce experimental measurements under various conditions. Here, after carefully exploring the impact of each simulation parameter on the final J-V curve, we report which one can stimulate the bump formation at scan rate 50 mV/s, which causes no bump in unencapsulated devices. Based on reasonable values[56,57], we varied the cation mobility by two orders of magnitude, from $2 \cdot 10^{-11}$ cm^2/Vs to $2 \cdot 10^{-9}$ cm^2/Vs. As a rule of thumb, according to Einstein's relation and the Arrheniuslike form of the diffusion coefficient, an increase by one order of magnitude in mobility would be achievable with a rather small (~0.06 eV) decrease in iodine vacancy migration barrier. For each mobility, we simulated the device response in reverse scan at 50 mV/s. The resulting J-V curves are shown in Fig. 8a. As previously reported, the bump does not appear at $2 \cdot 10^{-11}$ cm^2/Vs for this scan rate (it would appear for 6 mV/s) [11]. However, we found that an increase in cation mobility lowers the final J_{SC} and induces the bump earlier, i.e., at higher voltages, even at 50 mV/s. Notably, we find that this behaviour emerges regardless of the particular choice of other simulation parameters (see, e.g., Fig. S14), further supporting our hypothesis of an ion-induced origin of the bump.

To better understand the microscopic origin of this behaviour, we focused on how the electrostatic potential and electric field look across the device. The maximum in current, as one would expect, corresponds to a maximum in (positive) electric field in the bulk of the PSC, as seen in Fig. S15, where we plot the electric field ~1 μm away from the c-TiO_2 interface, in the mp-ZrO_2/perovskite layer. However, the most critical transport phenomena occur in the topmost 10 nm of the perovskite/mp-TiO_2 region, at the interface with c-TiO_2. Indeed, the electron extraction efficiency ultimately depends on the sign and magnitude of the local electric field $\vec{E}$ (i.e. negative derivative of the potential) at this interface. This can either favor (negative $\vec{E}$, pointing towards the interface) or hamper (positive $\vec{E}$, pointing away from the interface) cation accumulation in its proximity, thus modulating the local density of electrons. In Fig. 8b, we show the potential profiles in this region, at five applied voltages ranging from 0.5 V (yellow lines) to 0.1 V (red lines) and for an increasing cation mobility (left to right). In Fig. 8c, the resulting $\vec{E}$ at the c-TiO_2 interface (i.e. at x = 50 nm) is plotted as a function of the applied voltage and for the same values of cation mobility. We note that the local electric field $\vec{E}$ at $V=V_{OC}$ and $V=0$ reaches values two orders of magnitude larger than in the bulk (see Fig. S15). This is due to both the relatively huge generation rate of electron-hole pairs in this narrow region of the PSC (see Fig. S4) and the relatively high net ionic charge accumulating therein during the voltage scan. Most importantly, the electric field increases as the reverse scan proceeds, starting from being negative at $V=V_{OC}$ and eventually changing sign from negative to positive at the voltages where the reverse J-V curves exhibit the bump. This is due to a sign change of the net ionic density at the interface (Fig. S16), from being cation-rich (negative $\vec{E}$) to being anion-rich (positive $\vec{E}$), similar to what was reported to occur for $2 \cdot 10^{-11}$ cm^2/Vs at a scan rate of 6 mV/s [11]. This drastic change of interface polarization hampers further electron accumulation in the proximity of the interface and may thus be regarded as the root cause of the overall current suppression.

It is worth noting that the reversible degradation observed in the experiments, often characterized by a more pronounced decrease in J_{SC} along with the bump, is likely due to a complex interplay between water-induced ion mobility enhancement and other reversible degradation effects[57].

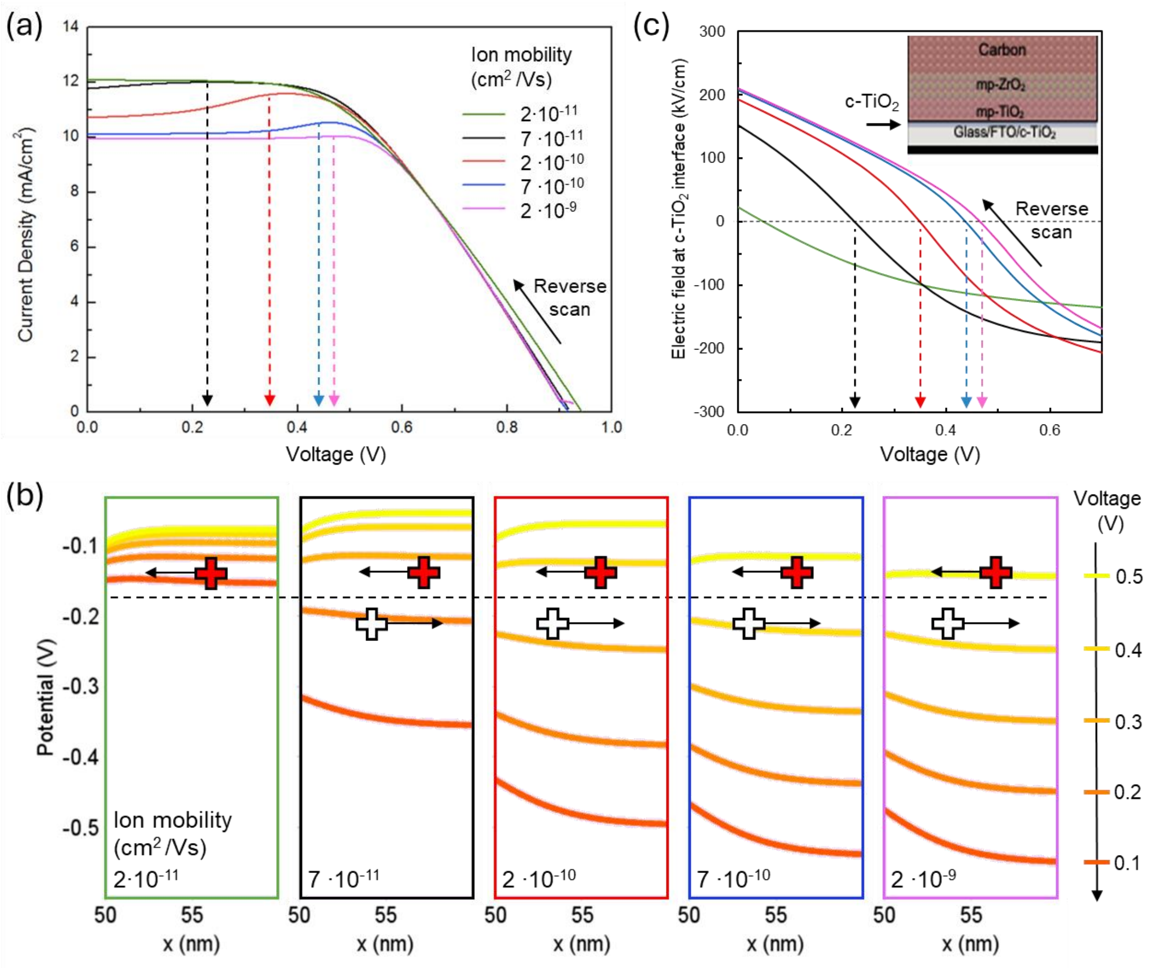

Fig 8 Effect of cation mobility on the reverse-scan J-V curves of AVA-$MAPbI_3$ mC-PSCs at fixed scan rate of 50 mV/s. (a) Simulated J-V curves for different values of cation mobility, exhibiting bumps at specific voltages (arrows). (b) Simulated potential profiles across the first 10 nm of the perovskite/mp-TiO_2 layer near c-TiO_2, for different applied voltages from 0.5V (yellow) to 0.1V (red). Panels from left to right show the evolution of the potential profiles for the different considered values of cation mobility. Red (white) plus signs schematically represent cations moving towards (away from) the c-TiO2 interface. (c) Electric field at the c-TiO_2 interface, switching sign at the same voltages where the "bumps" occur.

3.2.3 Atomistic correlations between a single water molecule and charged defects in $MAPbI_3$

The previous paragraph strongly indicates that the presence of the bump in the J-V curves of hybrid perovskite photovoltaic devices is related to an increase in the mobility of positively charged mobile ions in the presence of H_2O molecules. To better understand the possible interaction mechanisms between water molecules and charged defects in $MAPbI_3$, we performed density functional theory calculations in (2×2×2) pseudocubic $MAPbI_3$ supercells containing a single H_2O molecule and positively charged iodine vacancies (V_I^+) in various positions within the supercell (see Experimental section). It is important to point out here that iodide vacancies have low migration barriers[56] and tend to obtain a positive charge for the entire range of the electrochemical potential within the material's bandgap[58].

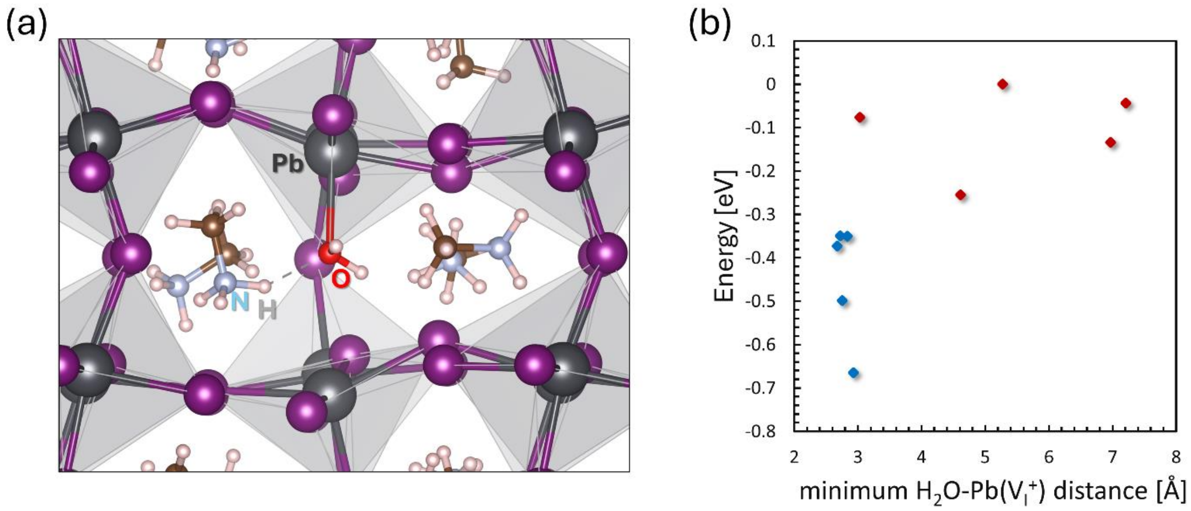

Fig 9 (a) Schematic representation of an H_2O molecule interacting with an undercoordinated Pb atom that stands next to a positively charged iodine vacancy in $MAPbI_3$. (b) Relative energy as a function of the minimum distance between an H_2O molecule and a Pb atom that stands next to charged iodine vacancy in $MAPbI_3$. Blue dots indicate atomic configurations where the H_2O molecule interacts with the dangling bond of the undercoordinated Pb atom, whereas red dots indicate configurations where there is no direct interaction. A total of 10 different configurations is considered.

Fig. 9a shows the most stable configuration obtained after structural relaxation, which is characterized by an interstitial H_2O molecule whose transient negative charge of the dipole (localized on the O atom) interacts with an undercoordinated Pb atom next to the V_I^+ site. When changing positions of the V_I^+ within the supercell, we observe that configurations where interactions near vacancy sites generally have lower energy with respect to configurations where it is distant from V_I^+ sites (Fig. 9b). Overall, we notice that two factors that influence the total energy of each configuration are: (a) the local deformations induced on the perovskite lattice, and (b), the possibility of charge sharing between H_2O and undercoordinated Pb atoms next to V_I^+ sites. Hence, considering the extremely low migration barriers reported for H_2O molecules within $MAPbI_3$[53], our results indicate that H_2O molecules should diffuse near charged iodide vacancies within the perovskite lattice, where the possibility of interacting with undercoordinated Pb atoms is higher, to minimize the total energy of the system. Although this aspect by itself cannot be directly correlated with the increase of iodine vacancy mobilities, it could indicate a plausible combined ionic diffusion mechanism that involves a simultaneous movement of both types of defects (V_I^+ and H_2O) within the PSC.

3.3 Polyurethane on mC-PSCs with Eu:$CsPbI_3$

As a further case study, we evaluated the encapsulation properties and behaviour of the thermosetting PU by applying it to mC-PSCs infiltrated with Eu:$CsPbI_3$ and monitoring the electrical performances over time. This fully inorganic formulation is of interest for indoor applications due to its bandgap being higher than that of AVA-$MAPbI_3$[4]. The PU dispensation procedure and device area are the same as the previous perovskite formulation (Fig. 10a-b). The Eu:$CsPbI_3$ mC-PSCs were stored under the same conditions as AVA-$MAPbI_3$ mC-PSCs. The J-V curves over time for the representative device from a batch of four Eu:$CsPbI_3$ mC-PSCs are shown in Figs. 10 c-d along with the photovoltaic parameters (V_{OC}, FF, J_{SC} and PCE) evolution measured in full-area devices (1.5 cm^2) (Fig. 10e-f-g-h-i). Statistical data are shown in Fig. S17. The initial efficiency value of the unencapsulated mC-PSC is 5%, consistent with the efficiency previously reported for large-area Eu:$CsPbI_3$ mC-PSCs[11]. The efficiency increases to 9.4% in small area Eu:$CsPbI_3$ mC-PSCs devices (0.04 cm^2)[9,11]. The unencapsulated mC-PSC exhibited poor stability, with the power conversion efficiency (PCE) values dropped from 5% to 0.1% within 1 h (t_{80}=15 min), primarily due to a significant decrease in the J_{SC} value. This degradation is attributed to the phase transition from the photoactive γ-black phase to the non-photoactive δ–yellow phase, triggered and catalysed by ambient humidity.

The encapsulated mC-PSC initially performs with lower efficiency compared to the unencapsulated counterpart (4% vs 4.98%), owing to lower values of V_{OC} (0.92 V vs 1.1 V) and FF (45.8% vs 50.2%), similar to the case-study of AVA-$MAPbI_3$ mC-PSCs. Positively, both V_{OC} and FF increase over time, as shown in Fig. 10e-f, eventually reaching values comparable to those of the unencapsulated mC-PSCs (1.03 V and 51.6%, respectively). We argue that this increase in V_{OC} and FF values is attributable to a maturation effect, reported elsewhere as due to a reorganization of the perovskite crystallites within the porous matrix[59]. The J_{SC} value is instead constant over time (9.2 mA/cm^2) (Fig. 10g). As a result, the efficiency of the encapsulated cell reaches a maximum efficiency of 5.1% after 220 h, overcoming the initial efficiency of the unencapsulated mC-PSC (5%), as shown in Fig. 10g. The encapsulated devices exhibit good long-term stability, retaining 80% of their initial efficiency for 250 h (Fig. 10h). This represents a 1000-fold stability improvement compared to the unencapsulated mC-PSCs, highlighting the beneficial effect of PU on enhancing the mC-PSC durability. The subsequent decline in efficiency is due to the phase transformation from the black to the yellow phase of Eu:$CsPbI_3$. The fact that the black Eu:$CsPbI_3$ phase starts transforming into the yellow phase (Fig. 10 and Fig.S18) at the same time when the bump appears in AVA-$MAPbI_3$ mC-PSCs (~250 h) (Fig. 1), further supports that the bump phenomenon is related to moisture diffusion through the PU and indeed to water molecules action. This also implies that using Kapton tape would be ineffective once water access has caused an irreversible phase transition in the perovskite layer.

We found that the durability of mC-PSCs based on Eu:$CsPbI_3$ is further enhanced by incorporating PU as a co-encapsulant between the device and a glass cover. Consequently, the t_{80} is extended to 1250 h, as illustrated in Fig. S19, representing a 5000-fold increase compared to the unencapsulated device. Focused edge-sealing strategies could further improve the stability of these devices[60,61].

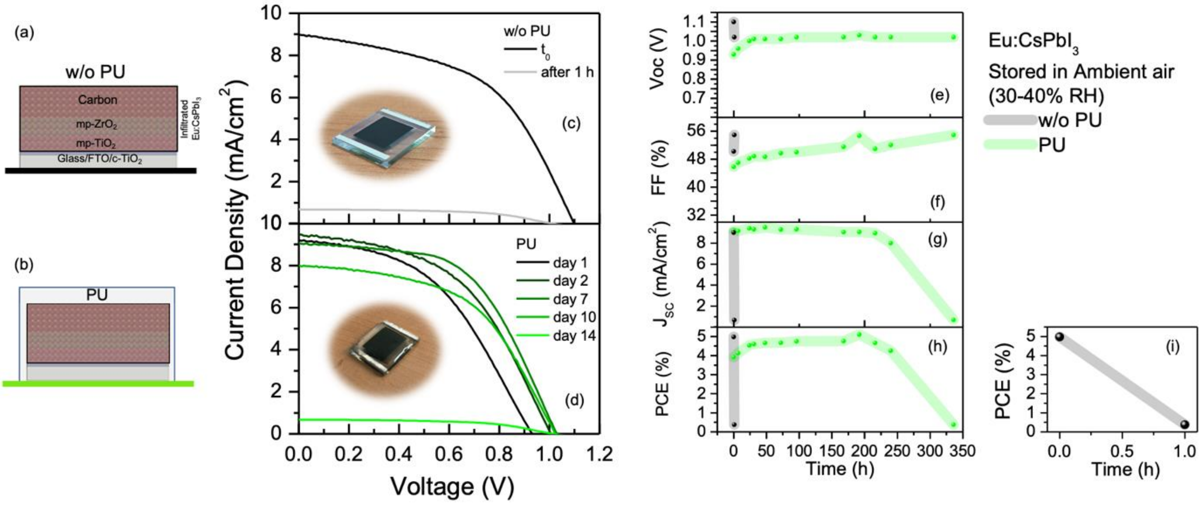

Fig 10 Schematic of the Eu:$CsPbI_3$ mC-PSC w/o PU (a) and with PU (b). J-V curves (reverse scan) over the time for Eu:$CsPbI_3$ mC-PSC w/o PU (c) and with PU (d). Evolution of V_{OC} (e), FF (f), J_{SC} (g) and PCE (h) over the time for $CsPbI_3$:$EuCl_3$ mC-PSC w/o PU and with PU. The efficiency of Eu:$CsPbI_3$ mC-PSC w/o PU (i) decreases from 5% to 0.1% in ~1 hour due to the phase transition of Eu:$CsPbI_3$ perovskite from black to yellow phase.

4. Conclusion

In conclusion, our study demonstrates the benefits of using thermosetting PU resin as an encapsulating layer (1.5 mm) to enhance the stability of mesoporous HTL-free perovskite solar cells based AVA-$MAPbI_3$ and Eu:$CsPbI_3$.

In the case of AVA-$MAPbI_3$ mC-PSCs, the devices encapsulated with PU and C tape+PU are characterised by the emergence of a bump in the J-V curves after 250 h of exposure in the air. The appearance of a bump, with a consequent inflation of FF and the decrease of J_{SC}, is reported in the literature for unencapsulated mC-PSCs analysed at a low scan rate (4-6 mV/s) in air conditions at 24 °C. In our case, the bump formation unexpectedly occurs at a high scan rate of 50 mV/s in encapsulated mC-PSCs stored in air (RH 30-40% 25 °C). Moreover, we show that bump formation is not linked to an interaction between PU and the mC-PSC surface, as inserting an interlayer of C-tape produced the same effect.

Counterintuitively, we found that the presence of the bump in PU-encapsulated mC-PSC is not indicative of material degradation within the device. The bump can be reset by storing the device under N_2 flow, leading to a recovery of the initial electrical performance. We also showed that unencapsulated and PU-encapsulated devices behave differently under high humidity conditions (RH 100% and in the temperature range 50-90 °C). In the first case, abundant and continuous water access produces large areas of deep degradation in the perovskite material, starting from the mC top contact and extending into the oxide layers at the ETL side. In the second case, no by-products are observed and indeed recovery of the initial electrical performance remains feasible. This demonstrates that PU serves as a protective layer, allowing limited water access into the device, likely through a dynamic equilibrium. This limited access to water molecules, which is known to cause an increase in cation mobility, was pinpointed as the root cause of the bump by simulating the ionic-electrical response of the devices. Without such a variation in mobility, the bump would only be detected at a low scan rate (4-6 mV/s). More generally, our simulations provide key insights into the microscopic physical origin of the bump, clearly attributing it to a variation of net ionic charge at the perovskite/mp-TiO_2 and c-TiO_2 interface, and the consequent change of interface polarization, which ultimately determines electron extraction.

Lastly, among different interlayers applied between mC-PSCs and PU, the use of a Kapton tape mitigates bump formation, and this has been linked to its higher hydrophobicity and reduced interaction with water molecules compared to PU alone. In this case, the t_{90} is extended to ~6000 h, a value 3-fold higher than that measured in unencapsulated devices (1965 h). The projected t_{80} is 10800 h. In addition, this encapsulation method prevents the transformation from $MAPbI_3$ to PbI_2 when the device is immersed in H_2O, preserving its photovoltaic performance.

In the case of Eu:$CsPbI_3$ mC-PSCs, while the unencapsulated sample shows a rapid decline in performance (t_{80}=15 min) due to phase transition induced by ambient humidity, PU-encapsulated devices exhibit significantly improved stability, retaining 80% of their initial efficiency for up to 250 h. This represents a 1000-fold increase in stability compared to their unencapsulated counterparts. Further encapsulation improvements, such as placing PU between the device and a glass cover, extend the device lifetime to 1250 h, resulting in a 5000-fold gain in stability.

Supporting Information

Photovoltaic parameters statistics over time for four AVA-$MAPbI_3$ mC-PSC PU-encapsulated and unencapsulated devices; J-V curves showing bump in unencapsulated (t0) at scan rate=6 mV/s and PU-encapsulated (800 h) devices at scan rate 50 mV/s; photovoltaic parameter trends over time for unencapsulated vs. C-tape-encapsulated AVA-$MAPbI_3$ mC-PSC; simulated carrier generation profile under 1 sun for AVA-$MAPbI_3$ mC-PSC; XRD of unencapsulated AVA-$MAPbI_3$ mC-PSC after 1500 hours in air; XRD pattern of AVA-$MAPbI_3$ mC-PSC with PU film peeled after 1500 hours in air; J-V curves in reverse scan for C-tape+PU encapsulated AVA-$MAPbI_3$ mC-PSC over time, before and after PU peeling; J-V curves of unencapsulated AVA-$MAPbI_3$ mC-PSC under H_2O vapor and N_2 storage; XRD of unencapsulated AVA-$MAPbI_3$ mC-PSC post-water and N_2 exposure; PU water absorption profile over time at room temperature; photovoltaic parameters statistics over time for AVA-$MAPbI_3$ mC-PSC devices with various interlayers; water wettability comparison for PU, C tape, and Kapton tape surfaces; water contact angle measurements for PU, C tape, and Kapton tape; J-V curves of unencapsulated device pre- and post-10 seconds H_2O soak; impact of traps and recombinations on the simulated J-V curves for different values of cation mobility; electric field near c-TiO_2 interface during reverse scan for varying cation mobilities; cationic density at c-TiO_2 interface during reverse scan for different cation mobilities; photovoltaic parameters statistics over time for Eu:$CsPbI_3$ mC-PSC devices; PU-encapsulated Eu:$CsPbI_3$ mC-PSC at t_0 and after 14 days in air; photovoltaic parameters evolution over time for Glass+PU encapsulated Eu:$CsPbI_3$ mC-PSC.

Acknowledgements

This study is a result of the research project "*nuovi Concetti, mAteriali e tecnologie per l'iNtegrazione del fotoVoltAico negli edifici in uno scenario di generazione diffuSa*" [CANVAS], funded by the Italian Ministry of the Environment and the Energy Security, through the Research Fund for the Italian Electrical System (type-A call, published on G.U.R.I. n. 192 on 18-08-2022) CUP B53C22005670005. A partial support for equipment was provided by the national project BEYOND NANO Upgrade (CUP G66J17000350007).

This work was partially funded by the European Union (NextGeneration EU), through the MUR-PNRR project SAMOTHRACE – Sicilian MicronanoTech Research and Innovation Center (ECS00000022, CUP B63C22000620005). The project "Selective Capture Of metals byPolymeric spongEs (SCOPE) - CODE 2022RYP9YT_PE3_PRIN2022, CUP: B53D23004480006 is also acknowledged.

This research acknowledges support from the Project CH4.0 under the MUR program "Dipartimenti di Eccellenza 2023–2027" (CUP D13C22003520001).

The authors thank Sebastian Ferranti (CNR-IMM) for the technical support and Demak Polymers for providing polyurethane precursors.

Graphical Abstract

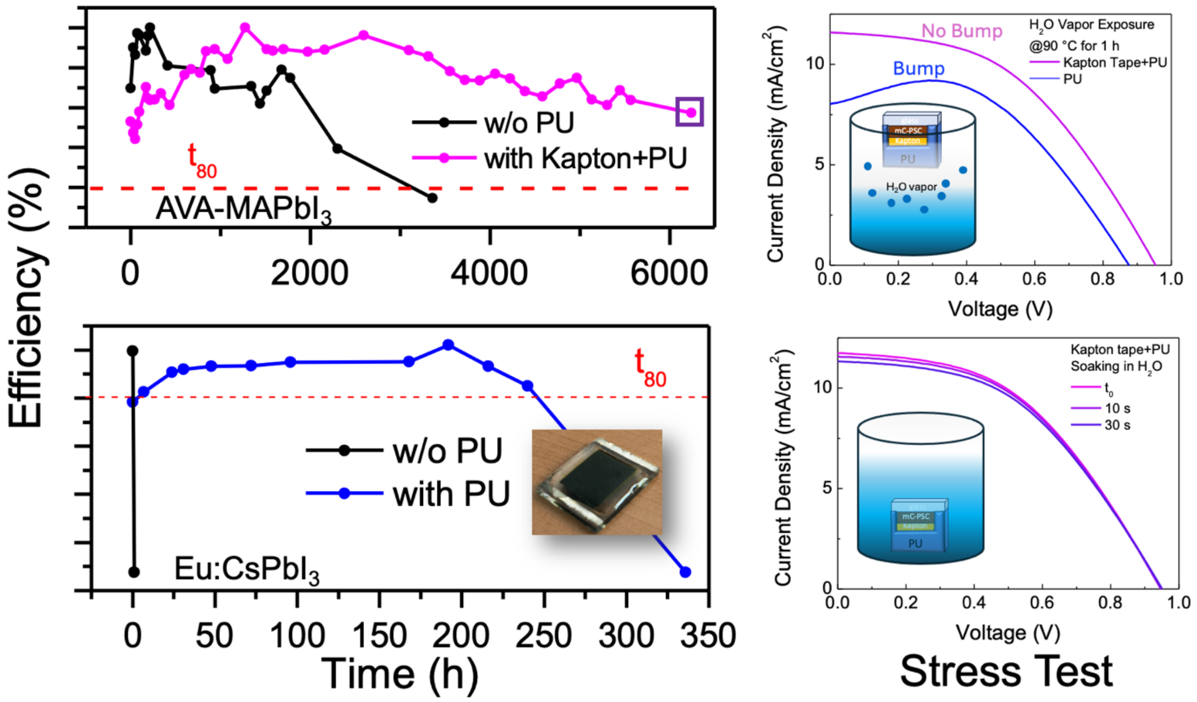

Left panels: durability of PU-encapsulated mesoporous carbon-based (mC) hole-transporting-layer-free (HTL-free) perovskite solar cells (PSC) integrating AVA-MAPbI$_3$ and Eu-CsPbI$_3$. Right panels: J-V curves after stress test under high humidity conditions for Kapton tape+PU and PU encapsulated PSCs or water immersion collected in PU-encapsulated HTL-free mc-PSC integrating AVA-MAPbI$_3$

References

---

[1] Jena, A. K.; Kulkarni, A.; Miyasaka, T. Halide Perovskite Photovoltaics: Background, Status, and Future Prospects, *Chem. Rev.* **2019**, *119*, 3036.

[2] Min, H. ; Lee, D. Y. ; Kim, J. ; Paik, M. J. ; Kim, Y. K. ; Kim, K. S. ; Kim, M. G.; Shin, T. J. ; Seok, S. I.; Perovskite solar cells with atomically coherent interlayers on SnO2 electrodes, *Nature* **2021**, *598*, 444.

[3] Meroni, S.M.P.; Worsley, C.; Raptis, D.; Watson, T.M. Triple-Mesoscopic Carbon Perovskite Solar Cells: Materials, Processing and Applications. *Energies* **2021**, *14*, 386. https://doi.org/10.3390/en14020386

[4] Zhanglin, G.; Jena, A.K.; Miyasaka, T. Halide Perovskites for Indoor Photovoltaics: The Next Possibility, *ACS Energy Lett.* **2023**, *8* (1), 90-95 DOI: 10.1021/acsenergylett.2c02268

[5] Valastro, S.; Mannino, G.; Smecca, E.; Bongiorno, C.; Sanzaro, S.; Deretzis, I.; La Magna, A.; Jena, A.K.; Miyasaka, T.; Alberti, A. Black-Yellow Bandgap Trade-Off During Thermal Stability Tests in Low-Temperature Eu-Doped CsPbI3 . *Sol. RRL*, **2022**, *6*: 2200008. https://doi.org/10.1002/solr.202200008

[6] Alberti, A.; Smecca, E.; Deretzis, I.; Mannino, G.; Bongiorno, C.; Valastro, S.; Sanzaro, S.; Fisicaro, G.; Jena, A.K.; Numata, Y.; Guo, Z.; Spinella, C.; Miyasaka, T.; La Magna, A. Formation of CsPbI3 γ-Phase at 80 °C by Europium-Assisted Snowplow Effect. *Adv. Energy Sustainability Res.* **2021**, *2*: 2100091.

[7] Mei, A.; Li, X.; Liu, L.; Ku, Z.; Liu, T.; Rong, Y.; Xu, M.; Hu, M.; Chen, J.; Yang, Y.; Grätzel, M.; Han, H. A hole-conductor–free, fully printable mesoscopic perovskite solar cell with high stability. *Science* **2014**, *345*,295-298. DOI:10.1126/science.1254763

[8] Hu, Y.; Si, S.; Mei A.; Rong, Y.; Liu, H.; Li, X.; Han, H. Stable Large-Area (10 × 10 cm2) Printable Mesoscopic Perovskite Module Exceeding 10% Efficiency. *Sol. RRL* **2017**, *1*: 1600019.

[9] Valastro, S.; Smecca, E.; Bongiorno, C.; Spampinato, C.; Mannino, G.; Biagi, S.; Deretzis, I.; Giannazzo, F.; Jena, A.K.; Miyasaka, T.; La Magna, A; Alberti, A. Out-of-Glovebox Integration of Recyclable Europium-Doped CsPbI3 in Triple-Mesoscopic Carbon-Based Solar Cells Exceeding 9% Efficiency. *Sol. RRL* **2022**, *6*: 2200267. https://doi.org/10.1002/solr.202200267

[10] Valastro, S.; Mannino, G.; Smecca, E.; Sanzaro, S.; Deretzis, I.; La Magna, A; Jena, A.K.; Miyasaka, T.; Alberti, A. Optical behaviour of γ-black CsPbI3 phases formed by quenching from 80 °C and 325 °C, J. *Phys. Mater.* **2021**, *4*, 034011

[11] Valastro, S., Calogero, G., Smecca, E., Bongiorno, C., Arena, V., Mannino, G., Deretzis, I., Fisicaro, G., La Magna, A. and Alberti, A., Performance Evaluation of Printable Carbon-Based Perovskite Solar Cells Infiltrated with Reusable CsPbI3:EuCl3 and Standard AVA-MAPbI3. *Sol. RRL* **2024**, 2300944. https://doi.org/10.1002/solr.202300944

[12] Dong, Q.; Liu, F. Z.; Wong, M. K.; Tam, H. W.; Djurišić, A. B.; Ng, A. N.; Surya, C.; Chan, W. K.; Ng, A. M. C. Encapsulation of Perovskite Solar Cells for High Humidity Conditions. *ChemSusChem* **2016**, *9*, 2597–2603, DOI: 10.1002/cssc.201600868

[13] Choi, E. Y.; Kim, J.; Lim, S.; Han, E.; Ho-Baillie, A. W. Y.; Park, N. Enhancing stability for organic-inorganic perovskite solar cells by atomic layer deposited Al2O3 encapsulation. *Sol. Energy Mater. Sol. Cells* **2018**, *188*, 37– 45,

[14] Cheacharoen, R.; Boyd, C.C.; Burkhard, G.F.; Leijtens, T.; Raiford, J.A.; Bush, K.A.; Bent, S.F.; McGehee, M.D. Encapsulating perovskite solar cells to withstand damp heat and thermal cycling, *Sustain. Energy Fuels* **2018**,*2*, 2398-2406

[15] Shi, Y.; Zhang, F. Advances in Encapsulations for Perovskite Solar Cells: From Materials to Applications. *Sol. RRL* **2023**, *7*: 2201123. https://doi.org/10.1002/solr.202201123

[16] Wang, Y.; Ahmad, I.; Leung, T.; Lin, J.; Chen, W.; Liu, F.; Ching Ng, A.M.; Zhang, Y.; Djurišić, A.B. Encapsulation and Stability Testing of Perovskite Solar Cells for Real Life Applications, *ACS Mater. Au* **2022**, *2*, 3, 215–236

[17] Matteocci, F.; Cinà, L.; Lamanna, E.; Cacovich, S.; Divitini, G.; Midgley, P.A.; Ducati, C.; Di Carlo, A. Encapsulation for long-term stability enhancement of perovskite solar cells, *Nano Energy* **2016**, *30*, 162-172

[18] Li, Z.; Xin Wu, Wu, S.; Gao, D.; Dong, H.; Huang, F.; Hu, X.; Jen, A. K.-Y.; Zhu, Z. An effective and economical encapsulation method for trapping lead leakage in rigid and flexible perovskite photovoltaics, *Nano Energy* **2022**, *93*, 106853

[19] Emery, Q.; Remec, M.; Paramasivam, G.; Janke, S.; Dagar, J.; Ulbrich, C.; Schlatmann, R.; Stannowski, B.; Unger, E.; Khenkin, M. Encapsulation and Outdoor Testing of Perovskite Solar Cells: Comparing

---

Industrially Relevant Process with a Simplified Lab Procedure, *ACS Appl. Mater. Interfaces.* **2022**, *14* (4), 5159-5167

[20] Valastro, S.; Smecca, E.; Mannino, G.; Bongiorno, C.; Fisicaro, G.; Goedecker, S.; Arena, V.; Spampinato, C.; Deretzis, I.; Dattilo, S.; Scamporrino, A.; Carroccio, S.; Fazio, E.; Neri, F.; Bisconti, F.; Rizzo, A.; Spinella, C.; La Magna, A.; Alberti, A. Preventing lead leakage in Perovskite solar cell with a sustainable titanium dioxide sponge, *Nat. Sustain.* **2023**, *6*, 974.

[21] Bisconti, F.; Giuri, A.; Dominici, L.; Carallo, S.; Quadrivi, E.; Biagini, P.; Listorti, A.; Corcione, C.E.; Colella, S.; Rizzo, A. Managing transparency through polymer/ perovskite blending: a route toward thermostable and highly efficient, semi-transparent solar cells. *Nano Energy* **2021**, *89,* 106406.

[22] Yang, B.; Zhang, M.; Qiao, G.; Zhang, H., Perovskite Solar Cells: Emerging Photovoltaic Technology for Achieving Net-Zero Emission Agrivoltaics Ecosystem. *Sol. RRL* **2023**, *7*: 2300217.

[23] Aydin, E.; Ugur, E.; Yildirim, B.K.; Allen, T.G.; Dally, P.; Razzaq, A.; Cao, F.; Xu, L.; Vishal, B.; Yazmaciyan, A.; Said, A.A.; Zhumagali, S.; Azmi, R.; Babics, M.; Fell, A.; Xiao C.; De Wolf, S. Enhanced optoelectronic coupling for perovskite/silicon tandem solar cells, *Nature* **2023**, *623*, 732–738

[24] Giuliano, G.; Bonasera, A.; Arrabito, G.; Pignataro, B. Semitransparent perovskite solar cells for building integration and tandem photovoltaics: design strategies and challenges. *Sol. RRL* **2021**, 5, 2100702.

[25] Liang, H.; Yang, W.; Xia, J.; Gu, H. ; Meng, X.; Yang, G.; Fu, Y.; Wang, B.; Cai, H.; Chen, Y.; Yang, S.; Liang, C. Strain Effects on Flexible Perovskite Solar Cells. *Adv. Sci.* **2023**, *10*, 2304733.

[26] Bisconti, F.; Leoncini,M.; Gambino, S.; Vanni, N.; Carallo, S.; Russo, F.; Armenise, V.; Listorti, A.; Colella, S.; Valastro, S.; Alberti, A.; Mannino, G.; Rizzo, A. Mimicking Natural Antioxidant Systems for Improved Photostability in Wide-Band-Gap Perovskite Solar Cells, *ACS Nano* **2024**, *18* (2), 1573-1581

[27] Zhang, D., Li, D., Hu, Y.; Mei, A.; Han, H. Degradation pathways in perovskite solar cells and how to meet international standards. *Commun. Mater.* **2022**, *3*, 58.

[28] Jacobsson, T. J.; Schwan, L. J.; Ottosson, M.; Hagfeldt, A.; Edvinsson, T. Determination of Thermal Expansion Coefficients and Locating the Temperature-Induced Phase Transition in Methylammonium Lead Perovskites Using X-ray Diffraction, *Inorg. Chem.* **2015,** *54* (22), 10678-10685

[29] Grancini, G.; Roldán-Carmona, C.; Zimmermann, I.; Mosconi, E.; Lee, X.; Martineau, D.; Narbey, S.; Oswald, F.; De Angelis, F.; Graetzel, M.; Nazeeruddin, M. K. One-Year stable perovskite solar cells by 2D/3D interface engineering. *Nat. Commun.* **2017**, *8*, 15684. https://doi.org/10.1038/ncomms15684

[30] Kobayashi E.; Tsuji, R.; Martineau, D.; Hinsch, A.; Ito, S. Light-induced performance increase of carbon-based perovskite solar module for 20-year stability, *Cell Rep. Phys. Sci.* **2021**, *2*, 12, 100648

[31] Kyranaki, N.; Perrin, L.; Flandin, L.; Planès, E.; Farha, C.; Wagner, L.; Saddedine, K.; Martineau, D.; Cros, S. Comparison of Glass–Glass versus Glass–Backsheet Encapsulation Applied to Carbon-Based Perovskite Solar Cells. *Processes* **2023**, *11*, 2742. https://doi.org/10.3390/pr11092742

[32] Fu, Z.; Xu, M.; Sheng, Y.; Yan, Z.; Meng, J.; Tong, C.; Li, D.; Wan, Z.; Ming, Y.; Mei, A.; Hu, Y.; Rong, Y.; Han, H. Encapsulation of Printable Mesoscopic Perovskite Solar Cells Enables High Temperature and Long-Term Outdoor Stability, *Adv. Funct. Mater.* **2019**, *29*, 1809129. https://doi.org/10.1002/adfm.201809129

[33] Raman, R. K.; Ganesan, S.; Alagumalai, A.; Sudhakaran Menon, V.; Gurusamy Thangavelu, S. A.; Krishnamoorthy, A. Rational Design, Synthesis, and Structure–Property Relationship Studies of a Library of Thermoplastic Polyurethane Films as an Effective and Scalable Encapsulation Material for Perovskite Solar Cells, *ACS Appl. Mater. Interfaces.* **2023**, *15* (46), 53935-53950

[34] Bonomo, M.; Taheri, B.; Bonandini, L.; Castro-Hermosa, S.; Brown, T. M.; Zanetti, M.; Menozzi, A.; Barolo, C.; Brunetti, F. Thermosetting Polyurethane Resins as Low-Cost, Easily Scalable, and Effective Oxygen and Moisture Barriers for Perovskite Solar Cells, *ACS Appl. Mater. Interfaces.* **2020**, *12* (49), 54862-54875

[35] Perrin, L.; Planes, E.; Shioki, T.; Tsuji, R.; Honore, J.-C.; Farha, C.; Ito, S.; Flandin, L. How Ammonium Valeric Acid Iodide Additive Can Lead to More Efficient and Stable Carbon-Based Perovskite Solar Cells: Role of Microstructure and Interfaces?. *Sol. RRL* **2024**, *8*: 2400393. https://doi.org/10.1002/solr.202400393

[36] Giannozzi, P.; Baroni, S.; Bonini, N.; Calandra, M.; Car, R.; Cavazzoni, C.; Ceresoli, D.; Guido, L. C.; Cococcioni, M.; Dabo, I. et al. QUANTUM ESPRESSO: a modular and open-source software project for quantum simulations of materials. *J. Phys.: Condens. Matter* **2009**, *21*, 395502.

[37] Chakraborty, D.; Berland, K.; Thonhauser, T. Next-generation nonlocal van der Waals density functional. *J. Chem. Theory Comput.* **2020**, *16*, 9, 5893–5911

---

[38] Perdew, J. P.; Burke, K.; Ernzerhof, M. Generalized Gradient Approximation Made Simple. *Phys. Rev. Lett.* **1996**, *77*, 3865.

[39] Vanderbilt, D. Soft self-consistent pseudopotentials in a generalized eigenvalue formalism. *Phys. Rev. B* **1990**, *41*, 7892.

[40] Monkhorst, H. J.; Pack, J. D. Special points for Brillouin-zone integrations, *Phys. Rev. B* **1976**, *13*, 5188.

[41] Planes, E.; Farha, C.; De Moor, G.; Narbey, S.; Perrin, L.; Flandin, L. Maturing Effects in Carbon-Based Perovskite Solar Cells: Understanding and Consequences on Photovoltaic Performances, *Sol. RRL* **2023**, *7*, 2300492.

[42] Zouhair, S.; Luo, B.; Bogachuk, D.; Martineau, D.; Wagner, L.; Chahboun, A.; Glunz, S.W.; Hinsch, A. Fill Factor Assessment in Hole Selective Layer Free Carbon Electrode-Based Perovskite Solar Cells with 15.5% Certified Power Conversion Efficiency, *Sol. RRL* **2022**, *6*, 2100745.

[43] Caddeo C.; Marongiu, D.; Meloni, S.; Filippetti, A.; Quochi, F.; Saba, M.; Mattoni, A.Hydrophilicity and Water Contact Angle on Methylammonium Lead Iodide, *Adv. Mater. Interfaces* **2019**, *6*, 1801173

[44] Leguy, A.M.A.; Hu, Y.; Campoy-Quiles, M.; Alonso, M.I.; Weber, O.J.; Azarhoosh, P.;van Schilfgaarde, M.; Weller, M.T.; Bein, T.; Nelson, J.; Docampo, P.; Barnes, P.R.F. Reversible Hydration of CH3NH3PbI3 in Films, Single Crystals, and Solar Cells, *Chem. Mater.* **2015**, *27*, 3397–3407

[45] Speight, J.; Lange's Handbook of Chemistry, **2005**, McGraw-Hill Education LLC

[46] Schlipf, J.; Bießmann, L.; Oesinghaus, L.; Berger, E.; Metwalli, E.; Lercher, J. A.; Porcar, L.; Müller-Buschbaum, P. In Situ Monitoring the Uptake of Moisture into Hybrid Perovskite Thin Films, *J. Phys. Chem. Lett.* **2018**, *9*, 2015–2021

[47] Fransishyn K.M.; Kundu, S.; Kelly, T.L. Elucidating the Failure Mechanisms of Perovskite Solar Cells in Humid Environments Using In Situ Grazing-Incidence Wide-Angle X-ray Scattering, *ACS Energy Lett.* **2018**, *3*, 2127–2133

[48] Sun, K.; Müller-Buschbaum, P., Shedding Light on the Moisture Stability of Halide Perovskite Thin Films. *Energy Technol.* **2023**, *11*: 2201475. https://doi.org/10.1002/ente.202201475

[49] Mai, C. T. K.; Halme, J.; Nurmi, H. A.; da Silva, A. M.; Lorite, G. S.; Martineau, D.; Narbey, S.; Mozaffari, N.; Ras, R. H. A.; Hashmi, S. G.; Vuckovac, M. Super-Droplet-Repellent Carbon-Based Printable Perovskite Solar Cells. *Adv. Sci.* **2024**, 2401016

[50] Song, Z.; Abate A.; Watthage S. C.; Liyanage G. K.; Phillips A. B.; Steiner U.; Graetzel M.; Heben M. J. Perovskite Solar Cell Stability in Humid Air: Partially Reversible Phase Transitions in the PbI2-CH3NH3I-H2O System. *Adv. Energy Mater.* **2016**, 6: 1600846. doi: 10.1002/aenm.201600846

[51] De Moor, G.; Charvin, N.; Farha, C.; Meyer, T.; Perrin, L.; Planes, E.; Flandin, L. Understanding the Anomalous *J–V* Curves in Carbon-Based Perovskite Solar Cells as a Structural Transition Induced by Ion Diffusion. *Sol. RRL* **2024**, *8*: 2300998.

[52] Aspiroz, J.M.; Mosconi, E.; Bisquert, J.; De Angelis F. Defect migration in methylammonium lead iodide and its role in perovskite solar cell operation, *Energy Environ. Sci.* **2015**, *8*, 2118-2127

[53] Jong, U.; Yu, C.; Ri, G.; McMahon, A.P.; Harrison, N.M Barnes, P.R.F.; Walsh A. Influence of water intercalation and hydration on chemical decomposition and ion transport in methylammonium lead halide perovskites, *J. Mater. Chem. A*, **2018**, *6*, 1067

[54] De Souza, R.A.; Kemp, D.; Wolf, M. J.; Ramadan, A. H. H. Caution! Static Supercell Calculations of Defect Migration in Higher Symmetry ABX3 Perovskite Halides May Be Unreliable: A Case Study of Methylammonium Lead Iodide, *J. Phys. Chem. Lett.* **2022**, *13* (49), 11363

[55] Setfos. Version 5.4. Fluxim AG (Switzerland). https://www.fluxim.com/setfos-intro

[56] Eames, C.; Frost, J.; Barnes, P.; O'regan, B.C.; Walsh, A.; Islam, M.S. Ionic transport in hybrid lead iodide perovskite solar cells. *Nat. Commun.* **2015**, *6*, 7497

[57] Thiesbrummel, J.; Shah, S.; Gutierrez-Partida, E.; Zu, F.; Peña-Camargo, F.; Zeiske, S.; Diekmann, J.; Ye, F.; Peters, K.P.; Brinkmann, K.O.; Caprioglio, P.; Dasgupta, A.; Seo, S.; Adeleye, F.A.; Warby, J.; Jeangros, Q.; Lang, F.; Zhang, S.; Albrecht, S.; Riedl, T.; Armin, A.; Neher, D.; Koch, N.; Wu, Y.; Le Corre, V.M.; Snaith, H.; Stolterfoht M. Ion-induced field screening as a dominant factor in perovskite solar cell operational stability. *Nat. Energy* **2024**, *9*, 664–676

[58] Xue, H.; Brocks, G.; Tao, S. First-principles calculations of defects in metal halide perovskites: A performance comparison of density functionals. *Phys. Rev. Mater.* **2021**, *5*(12), 125408.

[59] Hashmi, S.G.; Martineau, D.; Dar, M.I.; Myllymäki, T.T.; Sarikka, T.; Ulla, V.; Zakeeruddin, S.M.; Grätzel, M. High performance carbon-based printed perovskite solar cells with humidity assisted thermal treatment, *J. Mater. Chem. A* **2017**, *5*, 12060-12067

[60] Belich N.A.; Petrov, A.A.; Ivlev, P.A.; Udalova, N.N.; Pustovalova, A.A.; Goodilin, E.A.; Tarasov, A.B. How to stabilize standard perovskite solar cells to withstand operating conditions under an ambient

---

environment for more than 1000 hours using simple and universal encapsulation, *J. Energy Chem.* **2023**, *78*, 246-252

[61] Soares G.A.; Bicalho, I.S.; Castro-Hermosa, S.; Correa, L.D.; Miranda, B.H.; Marques, A.D.; Fernandes, S.L.; Cunha, T.G.; de Freitas, V.V.; Vilaça, R.D.; Wouk, L.; Bagnis, D. A comparative study of acrylic and epoxy-based adhesives for perovskite solar cells encapsulation, *Sol. Energy* **2024**, *273*, 112496